

TECHNISCHE
UNIVERSITÄT
DRESDEN

Investigation of the beta decay spectrum of ^{113}Cd with the COBRA experiment

Bachelor-Arbeit
zur Erlangung des Hochschulgrades
Bachelor of Science
im Bachelor-Studiengang Physik

vorgelegt von

Fabian Heiße
geboren am 24.02.1992 in Zschopau

Institut für Kern- und Teilchenphysik
Fachrichtung Physik
Fakultät Mathematik und Naturwissenschaften
Technische Universität Dresden

2013

Eingereicht am 10. Juni 2013

1. Gutachter: Prof. Dr. K. Zuber
2. Gutachter: Prof. Dr. M. Kobel

Summary

Abstract

English:

In this bachelor thesis the main goal is to investigate the fourfold forbidden, non-unique beta decay of the isotope ^{113}Cd . For this purpose, data from the COBRA experiment are used. In the following thesis, the data for this decay will be discussed as well as their accordance to common theories. The approach was to decide, under the usage of different comparison criteria, which data to use for further investigation. The next step was to create the final rate spectrum. Based on this spectrum, the important values for beta decay Q_β – value = (323.6 ± 1.2) keV and the half-life $T_{\frac{1}{2}}(^{113}\text{Cd}) = (7.91 \pm 0.22) \cdot 10^{15}$ years are found. These values fit very well to the theory and other experimental results. Furthermore the shape of the spectrum is in good accordance to the predicted theory throughout the whole region ($50 \text{ keV} < E_{\text{kin}}(\text{electron}) < 350 \text{ keV}$). There are however some unanswered questions such as the behavior of the rate spectrum in the low energy region down to $E_{\text{kin}}(\text{electron}) = 0 \text{ keV}$. On the whole this bachelor thesis makes a proposal to understand this fourfold forbidden beta decay better.

Abstract

Deutsch:

In dieser Bachelor-Arbeit ist das Hauptziel den vierfach verbotenen Betazerfall von ^{113}Cd zu untersuchen. Für diesen Zweck wurden Daten vom COBRA-Experiment in Italien genutzt. In der folgenden Arbeit wird das Betazerfallsspektrum genauso diskutiert, wie die Übereinstimmung dieses Spektrums mit dem von der Theorie erwarteten Spektrum. Nach der Untersuchung der Daten wurde ein finales Spektrum erstellt, anhand dessen dann die charakteristischen Größen für den Betazerfall berechnet wurden. In Bezug auf das finale Spektrum ergab sich für den Endpunkt des Spektrums folgender Wert: $Q_\beta = (323.6 \pm 1.2)$ keV. Außerdem erhält man für die Halbwertszeit von ^{113}Cd den Wert von $T_{\frac{1}{2}}(^{113}\text{Cd}) = (7.909 \pm 0.223) \cdot 10^{15}$ Jahren. Diese Werte stimmen sehr gut mit den Literaturwerten überein. Des Weiteren entspricht das Profil des Spektrums weitgehend dem theoretisch erwarteten Profil in einem weiten Bereich ($50 \text{ keV} < E_{\text{kin}}(\text{Elektron}) < 350 \text{ keV}$). Trotzdem bleiben noch offene Fragen, zum Beispiel welche Form das Betaspektrum im Bereich sehr kleiner kinetischer Energien des Elektrons hat (bis zu $E_{\text{kin}}(\text{Elektron}) = 0 \text{ keV}$). Zusammenfassend versucht diese Bachelor-Arbeit einen Ansatz für das bessere Verstehen des vierfach verbotenen Betazerfalls aufzuzeigen.

Contents

1	Introduction	7
2	Theoretical and experimental background	9
2.1	Theory for the beta decay of ^{113}Cd	9
2.1.1	The beta decay	9
2.1.2	Predicted spectrum for the beta decay	11
2.2	Experimental background	13
2.2.1	Experimental results for the beta spectrum of ^{113}Cd	13
2.2.2	Experimental setup	13
2.2.3	CdZnTe detectors	14
2.2.4	Calibration	14
3	Data analysis	15
3.1	Data background	15
3.2	Cuts	16
3.2.1	Z-distribution	16
3.2.2	Energy	17
3.3	Z-distribution	17
3.4	Rate spectrum	19
3.5	Rate versus run period	21
3.6	Final spectrum and conclusion	22
4	Results	25
4.1	Resolution of the detectors	25
4.2	Shape fit	25
4.3	Fit results	26
4.4	Half-life	27
4.5	Conclusion	29
5	Summary and outlook	31

6	References	33
6.1	Books and papers	33
6.2	World Wide Web	34
7	Appendix	35
7.1	Formulas for statistics	35
7.2	Formula for Gaussian propagation of uncertainties	35
7.3	Fit parameters	36
7.4	Table 7.1 – Masses for the natural elements of the detectors	36
7.5	Table 7.2 – Masses of the detectors	37
7.6	Table 7.3 – Rate trends of the detectors	38
7.7	Table 7.4 – Tabulated values of the Fermi function	39
7.8	Table 7.5 and 7.6 – Resolution of the detectors	40
7.9	Table 7.7 – Energy calibration uncertainties of the detectors	42

1 Introduction

The COBRA experiment (**C**admium **Z**inc **T**elluride **0**-Neutrino **D**ouble-**B**eta **R**esearch **A**pparatus) at the Laboratori Nazionale del Gran Sasso (LNGS) in Italy is one of the world's leading experiments in neutrino physics. The setup 1400 meters below earth's surface presents the perfect place to measure the weakly interacting neutrinos. Thus this setup could find an answer to the important question of the neutrino-less double beta decay [CEORG].

The detectors for this reaction contain cadmium, zinc and tellurium. The element cadmium, especially the isotope ^{113}Cd , is responsible for the significant background of the spectrum in the low energy region. This spectrum is caused by the fourfold forbidden beta decay of ^{113}Cd and is the subject of some other experiments to verify the quite complex theory for this spectrum (^{115}In and ^{50}V are the only other isotopes known to have such a highly forbidden transition beta decay).

The goal of this thesis is to investigate the shape for the ^{113}Cd beta decay spectrum and, based on this, important values like the half-life and the Q_β -value of this isotope. The theory as well as most of the experimental results for this topic can be found in the second chapter. The analysis of separate detectors for different comparison criteria, such as the interaction depth distribution and rate versus run period, is given in the third chapter. Finally the results are described in chapter four. Moreover in the same chapter calculations for the Q_β -value and half-life based on the analysis are presented. Furthermore the aim of this thesis is to give a first idea to better understand the characteristics of all 32 detectors and the comparison to each other under different criteria.

Lastly this thesis is also a first step to understand the behavior of the COBRA detectors and it offers new and unknown aspects for further investigations to learn more about the properties of neutrinos.

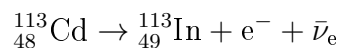
2 Theoretical and experimental background

For the understanding of the beta decay and the theory behind it, the following chapter presents a small summary of the theoretical fundamentals and the state of art in the experimental achievement in this field.

2.1 Theory for the beta decay of ^{113}Cd

2.1.1 The beta decay

The beta decay is one of three main reactions in a nucleus for emitting radiation. The other two are alpha decay and gamma rays. There are two types of beta decay: beta plus decay (β^+ decay) and beta minus decay (β^- decay). Both are caused by the weak force. In the beta plus decay a positron and an electron neutrino are set free during reaction by exchanging a W^+ boson, whereas at the beta minus decay an electron and an electron anti-neutrino are set free by the exchange of a W^- boson, referring to [wbeta]. In this thesis the beta minus decay of ^{113}Cd will be investigated. During the beta decay of ^{113}Cd the following reaction takes places in the nucleus:



That means that during a beta decay a neutron converts into a proton; more exactly: a down quark converts into an up quark through the weak force and sets an electron and an electron anti-neutrino free. In terms of the quantum flavor dynamics, or more generally the electroweak theory, the beta decay can be written as shown in Figure 2.1.

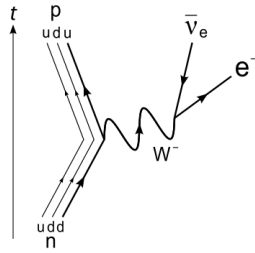


Figure 2.1: Feynman diagram for the beta minus decay ([Fgobd])

It is obvious that the beta decay is a three product reaction (daughter nucleus, electron and electron anti-neutrino). For this reaction the energy and the momentum have to be conserved. Therefore the emitted electron has a spectrum of energy after the reaction, because on the one hand there is a fixed energy which is released and there are three particles which can record the energy. On the other hand, the momentum is also conserved; hence the electron does not have a fixed energy after the decay. This energy spectrum for the electron is called the beta spectrum. There is of course a similar spectrum for the electron anti-neutrino; this is harder to measure, but it is possible to calculate it with the help of the electron spectrum. A more exact definition of the beta decay of ^{113}Cd is to include the differences of the parity and the spin from the nucleus in the description before the reaction (^{113}Cd) and the nucleus after the beta decay (^{113}In). In this nomenclature the beta decay from ^{113}Cd is called a fourfold forbidden beta decay, because the nucleus at the ground state from ^{113}Cd has a spin (J) and a parity (P), equal to $J^P = \frac{1}{2}^+$. For ^{113}In it is $J^P = \frac{9}{2}^+$. This shows that there is a transition from $\Delta J = 4$, and P is conserved. Therefore the β^- -decay of ^{113}Cd is named fourfold forbidden, non-unique β^- -decay. ^{113}Cd has a long half-life ($T_{\frac{1}{2}}$) of around 10^{15} years, because of $\Delta J = 4$. Moreover it is important that ^{113}Cd decays 100% of the time via beta decay to ^{113}In .

2.1.2 Predicted spectrum for the beta decay

In the “Table of Isotopes” ([ToICd]) exists a predicted shape for the allowed beta decay. That means a transition, where $\Delta J = 0; \pm 1$ and where the parity is conserved. This shape is shown in Figure 2.2.

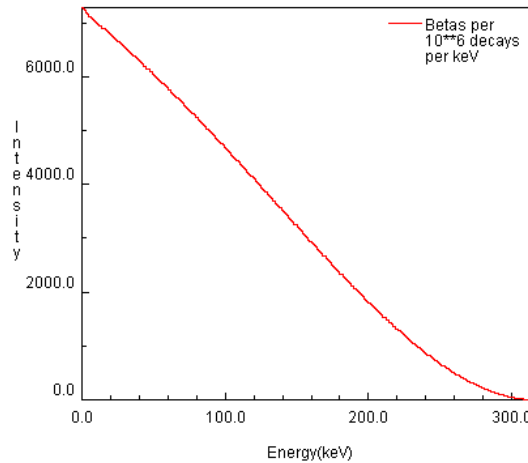


Figure 2.2: Predicted theoretical shape for the allowed beta decay of ^{113}Cd ([ToIalb])

For the fourfold forbidden beta decay of ^{113}Cd this spectrum needs to be multiplied by a correction factor ($C(\omega)$). The shape of the fourfold forbidden beta decay is predicted by the following formula for the energy distribution for the electrons with momentum p ([BJ69] and [SH66])¹:

$$N(p_e) dp_e = \frac{g^2}{2\pi^3} \cdot p_e^2 \cdot p_\nu^2 \cdot F(Z, W_e) \cdot C(W_e)$$

In this equation p_e is the electron momentum, $W_e = \sqrt{p_e^2 + 1}$ is the total energy of the electron, W_0 is the maximum value of W_e (this is the maximum total energy of the electron of the beta decay²), $p_\nu = W_0 - W_e$ the energy of the neutrino³, $F(E, Z)$ is the Fermi function and Z the atomic number of the daughter nucleus. Hence the theoretical shape of the beta decay is described by the subsequent formula:

$$s(p_e) = \text{const} \cdot p_e^2 \cdot F(Z, W_e) \cdot p_\nu^2 \cdot C(p_e) \quad (2.1)$$

where $p_e = \sqrt{(W_e)^2 - 1}$ is the momentum of the electron, const is a constant factor for adapting our measured spectrum to the theoretical shape and $C(p_e)$ is the correction factor. For this correction factor, a few models exist. The equation for $C(p_e)$ proposed by [BJ69] is

¹ All energies are in units of $m_e c^2$ and momenta in units of $m_e c$.

² Therefore the maximum kinetic energy of the electron is $W_0 - 1$. This energy is equal to the Q_β -value of the beta decay.

³ The mass of the electron anti-neutrino is smaller than 2.2 eV, referring to [wneum] and the energy resolution is in the region of 5 keV; hence the assumption for the mass-less electron anti-neutrino has been made.

quite complex and extensive. There are some other approaches for calculating $C(p_e)$ and in this thesis the following will be used (according to [BD94A],[FAD96] and [PB07]):

$$C(p_e) = p_e^6 + 7a_1 \cdot p_e^4 \cdot p_\nu^2 + 7a_2 \cdot p_e^2 \cdot p_\nu^4 + a_3 \cdot p_\nu^6 \quad (2.2)$$

For the Fermi function $F(E, Z)$ discrete values from Table 7.4 are used. Therefore $F(E, Z)$ is obtained by interpolating the values from Table 7.4 by a spline function. In sum the two Equations (2.1) and (2.2) describe the theoretical shape of the beta decay and are later used for fitting the data.

Up to the present there is only one predicted shape for the spectrum of this fourfold forbidden beta decay of ^{113}Cd which used another ansatz. The theoretical results from M.T. Mustonen and J. Suhonen are presented here and later compared to the experimental results from the COBRA experiment. Mustonen and Suhonen used for their theory the nuclear shell model and the proton neutron microscopic quasiparticle phonon model (pnMQPM). Based on this theory they calculated $T_{\frac{1}{2}} = 16.9 \cdot 10^{15}$ years. In Figure 2.3 the predicted theoretical spectrum of beta decay of ^{113}Cd is shown.

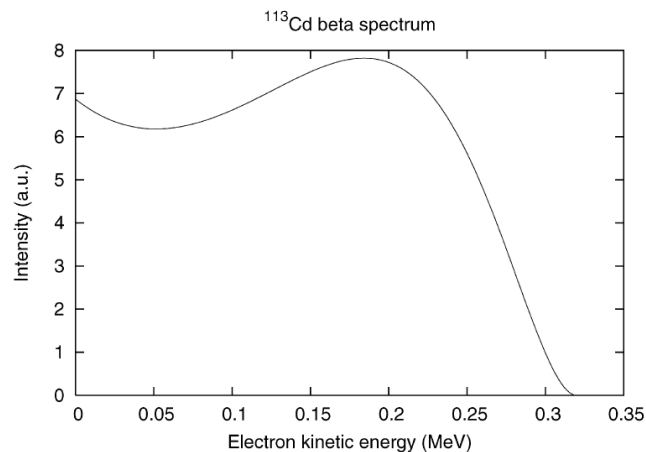


Figure 2.3: Predicted theoretical shape for the fourfold forbidden beta decay of ^{113}Cd ([MS07])

2.2 Experimental background

2.2.1 Experimental results for the beta spectrum of ^{113}Cd

There are a few experiments which have already measured $T_{\frac{1}{2}}$ and the Q_{β} -value for the fourfold forbidden beta decay of ^{113}Cd . For an overview, these results have been listed in Table 2.1 including uncertainties:

$T_{\frac{1}{2}}$ [10^{15} years]	Q_{β} [keV]	Source
7.7 ± 0.3	316 ± 3	Table of Isotopes [ToiCd]
8.04 ± 0.05	321.924 ± 0.839	Live Chart of Nuclides [LCoNCd]
8.00 ± 0.11 (stat)	322.2 ± 0.3 (stat) ± 0.9 (sys)	An Investigation into the ^{113}Cd Beta Decay Spectrum [BDSKZ]
	320 ± 3	The AME2003 atomic mass evaluation [AME03]
9.3 ± 0.5 (stat) ± 1 (sys)	318.8 ± 1.4 (stat) ± 5 (sys)	Large calorimetric devices for double beta decay and dark matter [BD94A]
8.04 ± 0.05	344.9 ± 0.2 (stat) ± 21 (sys)	Investigation of beta decay of Cd^{113} [PB07]
7.7 ± 0.3	337.4 ± 0.3 (stat) ± 22 (sys)	Beta decay of ^{113}Cd [FAD96]
8.23 ± 0.29 (stat)	320.45 ± 0.28 (stat)	Background Studies for the COBRA Experiment [RCOB09]
	321.9 ± 2.2	Mass difference [LCoNCd] $Q_{\beta} = m(^{113}\text{Id}) - m(^{113}\text{Cd})$
	322.571 ± 0.790	Atomic mass evaluation [AME12]

Table 2.1: Experimental results for the Q_{β} -value and $T_{\frac{1}{2}}$ for the beta decay of ^{113}Cd

The last entry is the most precise value, because the masses were measured with very sensitive penning traps.

2.2.2 Experimental setup

For collecting the data, CdZnTe semiconductor detectors from the COBRA experiment were used. They are situated inside of an inner copper shield (5 cm thickness), which is walled by a lead castle (20 cm thickness). A Faraday cage, which itself is protected by a neutron shield (7 cm thick boron loaded polyethylene plates and 20 cm of paraffin wax), encases this whole system. The whole experiment is situated in Laboratori Nationalidel Gran Sasso (LNGS) with 1400 m of rock shielding (3500 m water equivalent).

2.2.3 CdZnTe detectors

The CdZnTe detectors were produced by eV-PRODUCTS [evDet]. The detectors are CoPlanar Grid (CPG) devices [CPG95] with gold anode grids and a cathode. All detectors are covered with a passivated paint for a highly resistive surface layer and for long-term stability. The detectors are connected to high voltage foils with a low activity copper loaded glue.

An event in the detectors is reconstructed from two electronic signals (from anode and cathode), read out by the electronic system. Their functional principles are similar to a Frisch grid in a wire chamber. Every detector has an individually tailored high voltage, grid bias and weighting of the CPG subtracted signal, also called “difference signal”. The dual signals from CPGs allow a reconstruction of the interaction depth, the distance between anode and cathode.

2.2.4 Calibration

Calibration measurements were carried out on twelve dates for layer 1 and on five dates for layer 2, referring to Table 7.6. The energy of a photon from a ^{228}Th gamma source is used for the calibration energy of $E = 239$ keV. The photon is emitted by the following reaction. ^{212}Pb decays over β^- -decay to an excited state of ^{212}Bi . This excited state releases a photon with the energy $E = 239$ keV under de-excitation to the ground state of ^{212}Bi .

For the energy $E = 511$ keV the β^+ -decay of ^{22}Na is used. The positron, that is emitted by this transition, annihilates with another electron and releases the energy $E = 1022$ keV. The energy is deposited in form of two equal energy photons, which are emitted diametrically from the source because of the momentum conservation. One of these photons is collected and measured in the detectors, according to [BDSKZ].

3 Data analysis

For reaching the aim to calculate the Q_β -value and the half-life of the ^{113}Cd beta decay, it is important to study the existing data. It has to be decided which data of the different detectors will be included in the final beta decay spectrum. Therefore decision criteria have to be defined. All detectors will be compared to these criteria, to figure out what regular behavior is, and which detectors non-physical events collect. This is important, because these two irregularities spoil the spectrum and the calculations based on it. The assumption is that these non-physical events are different for different detectors. It is based on experience that some detectors collect more non-physical events than others and these non-physical events look different in different detectors. The following sections explain these criteria and point out their results.

3.1 Data background

For analyzing the ^{113}Cd beta decay the data from the first 32 CdZnTe semiconductor detectors of the COBRA experiment are used. The volume of each detector is 1cm^3 . The number content of cadmium in every detector is given by $(45.5 \pm 1 \text{ (sys)})\%$ ([BDSKZ]) and their individual masses are listed in Table 7.2. The detectors are arranged in two layers. Layer 1 carries detectors 1 - 16 and layer 2 detectors 17 - 32. The data were taken in an era where the detectors of layer 1 all run together 88 run periods from December 27th, 2011 to November 26th, 2012. The layer 2 detectors run 48 run periods, except detector 23, which never runs and detector 9, which runs only 45 run periods. All in all there are around $50 \text{ kg} \cdot \text{days}$ of data included in the whole analysis. It needs to be mentioned that the layer 2 detectors have on average a higher energy threshold. According to this, their rate spectrum begins at higher energies, and they have collected fewer total events due to their shorter total run time.

3.2 Cuts

To analyze the data, two data cuts have been applied, the so called standard cuts:

“flag_bad_pulse” and “flag_above_thresh”. The cut “!flag_bad_pulse” removes the signals which do not look like they came from a particle interaction. This cut removes the electronic disturbances. The second cut makes sure that there are no events with a total energy that is smaller than the adjusted threshold. This cut guarantees that events which are included represent a uniform sampling of the full z-range of the detector. This is important, because the true energy threshold is z-dependent, referring to [AMDFZ].

3.2.1 Z-distribution

In Figure 3.1 the interaction depth for the typical detectors 4 and 11 is shown for all run periods. The z-distribution represents the interaction depth: $z = 0$ is the anode and $z = 1$ is the cathode.

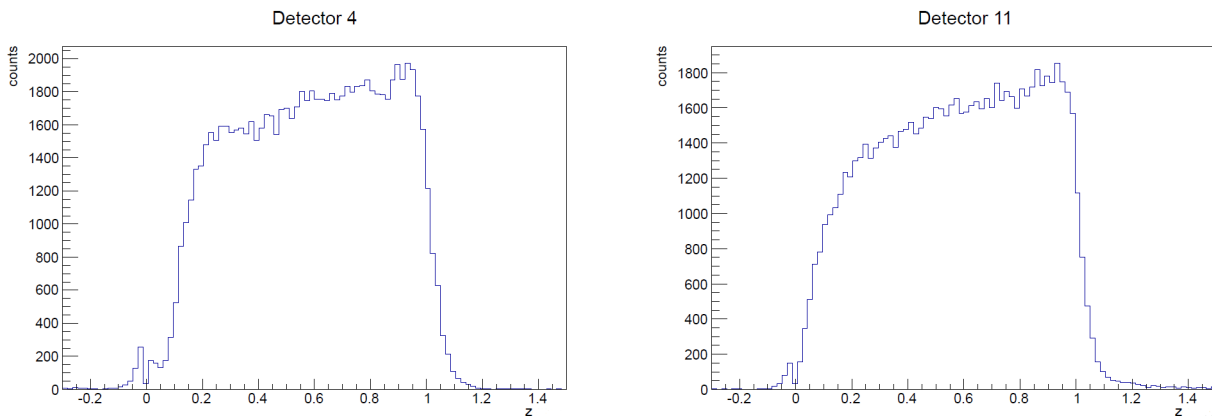


Figure 3.1: Z-distribution of detector 4 (left) and detector 11 (right)

Beside the two standard cuts, a lower and an upper limit for the total energy of the electron ($100 \text{ keV} < E < 350 \text{ keV}$) has been implemented, which will be explained in the next section. In both images the double energy effect near $z = 0$ is visible. That means, in this region the events are distorted, because they are too close to the anode, referring to [AMDFZ]. To reject these non-physical events a $z > 0.07$ -cut is implemented. In the left image there are some events with a $z > 1$. The reason is that there is an uncertainty in z-measurement, caused by the resolution of the detector. Therefore the z-selection should exceed $z = 1$ by a small amount comparable to the resolution. If a detector has a lot of events above $z = 1$, they should be rejected as non-physical or distorted. To minimize the uncertainty of this effect, an upper limit is also set for z: the $z < 1.02$ -cut.

3.2.2 Energy

Figure 3.2 shows the rate spectra from typical detectors over all run periods. It indicates that there is a low rate above an energy of 350 keV; most of this energy is induced by the rate of other isotopes. Therefore the decision was made to apply an upper limit for the energy: $E < 350$ keV. Another reason for this is that the theoretical end point of the investigated spectrum is at $E \approx 320$ keV; in no experiment a higher Q_{β} -value than $Q_{\beta} = 345$ keV is measured, referring to chapter 2 section 2.2.1 “Experimental results”. In Figure 3.2 the x-axis represents the measured energy of the electron in keV (the neutrino leaves the detector without detection).

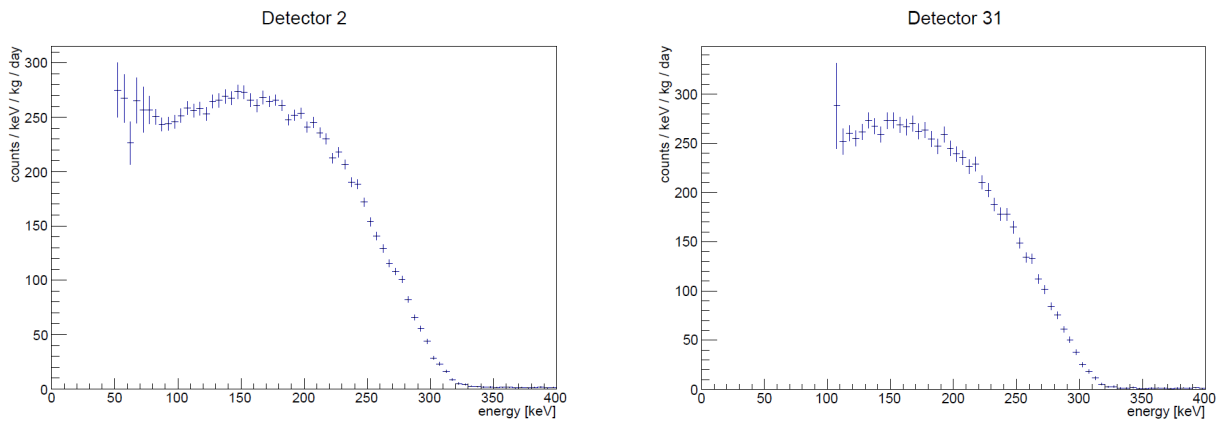


Figure 3.2: Rate spectra of detectors 2 and 31

3.3 Z-distribution

In this section the different z -distributions of the detectors are discussed. Every distribution was compared to each other. In this way it was possible to figure out what a regular shape is and where electronic disturbances may exist. In Figure 3.3 a selection of z -distributions is presented; some show a normal shape (detector number 1) and some show different evidence for non-physical events (detectors 3, 16 and 20).

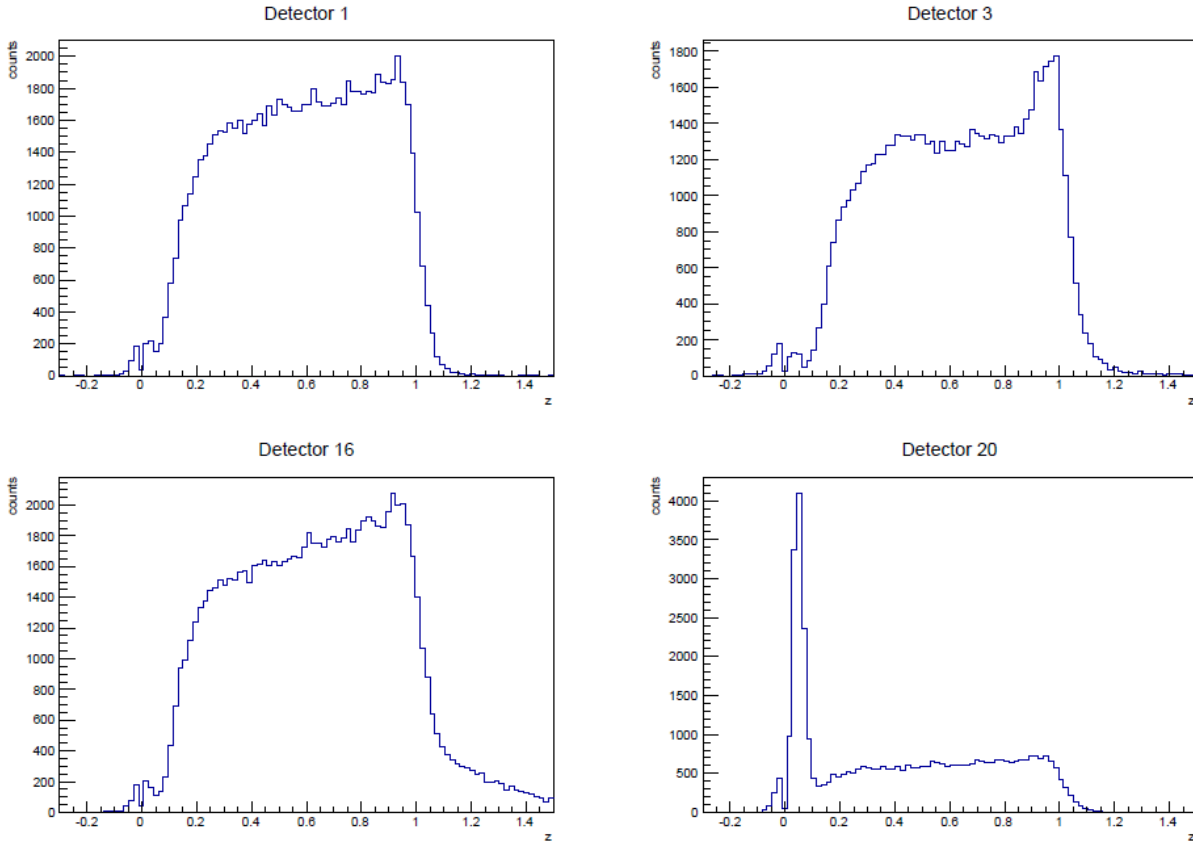


Figure 3.3: Z-distributions of detectors 1, 3, 16 and 20

The first image of detector 1 shows a regular behavior. Near $z = 0.0$ double energy peaks (which later are removed by our z -cut) appear. Furthermore the images show a high increase of counts until $z \approx 0.2$ and then a linear increase until $z \approx 0.95$. Because of the event reconstruction, the event depth is shifted to higher values. Shortly beyond $z = 1.0$ there is an abrupt decrease to under 200 counts and for $z = 1.2$ it has decreased almost below 10 counts (smaller than 1%).

The z -distribution of detector 3 has an abnormal shape. The regions of $z \approx 0$ and $z > 0.9$ look quite normal, but in the region between $0.4 < z < 0.8$ there is a flat region and then a very strong increase at $0.85 < z < 0.95$. The same behavior is shown by detector number 30. The reason for this behavior is the effect of “shared charge” events caused by too low grid bias. Detector numbers 9, 13 and 17 show an abnormal shape, too. This indicates problems within these detectors, which distort the event reconstruction. These reasons are motivation for not using these detectors for the final spectrum, because they could have some data with non-physical background.

The z -distribution of detector number 16 has a regular form below $z < 1.0$. However for $z > 1.0$ many more events are counted than in the z -distribution of a normal detector. These are obviously non-physical events or events that are shifted to such high z , caused by electronic disturbances, which escape the data cleaning cut. Therefore this detector is also not good in

terms of the regular z -distribution.

The last z -distribution of detector number 20 shows a very high peak in the region of $0 < z < 0.1$. Other investigations show that this is caused by only three of the run periods, where something undefined produced such a high event rate of non-physical events at this area of the z -distribution. Thus detector 20 will not be included in further analysis.

3.4 Rate spectrum

Another criterion for comparing the detectors among each other is looking at their rate spectra. To manage this task, a preliminary rate spectrum has been prepared. For this spectrum all the detectors are treated as one big detector (Table 7.2 is used for the average mass). This average spectrum (red dots) and the spectrum of every single detector (blue dots) is comprised in one image. In this way, it is visible what the regular behavior looks like and it is easier to figure out where abnormal forms are. Figure 3.4 shows again a selection of one normal detector (number 5) and detector numbers with non-regular spectra (detectors 3, 15 and 30).

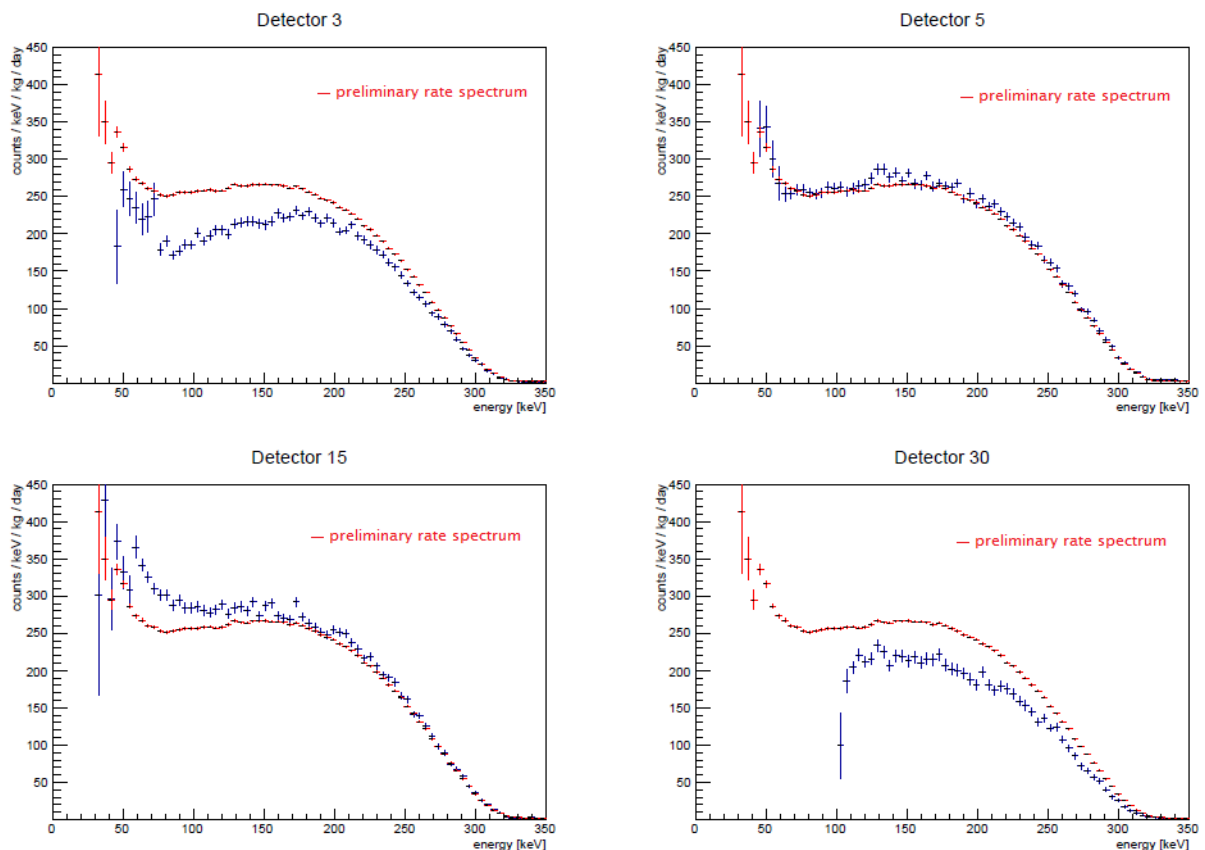


Figure 3.4: Rate spectra of detectors 3, 5, 15 and 30

The red average rate spectrum shows big error bars (include only statical fluctuations) from $0 \text{ keV} < E < 55 \text{ keV}$, because of an insignificant quantity of data in this energy region. From

$E \approx 35$ keV to $E = 81$ keV the rate decreases; it shows an increase of around 5.6% in the region from this local minimum to $E \approx 150$ keV. After this maximum the rate strongly decreases until $E = 350$ keV. According to this, the rate spectrum of the beta decay for ^{113}Cd can be classified into three sections, which are used for describing the single spectra: the low energy region ($35 \text{ keV} < E < 81 \text{ keV}$), the “dip region” ($81 \text{ keV} < E < 150 \text{ keV}$) and the “shoulder” of the spectrum ($150 \text{ keV} < E < 350 \text{ keV}$).

In the first image of Figure 3.4 the rate spectrum of detector number 3 is plotted. Over the whole energy range this detector has a lower rate. In the “dip region” the rate is up to a third lower than the average rate. Only at the end of the shoulder ($270 \text{ keV} < E < 350 \text{ keV}$) the rate of detector number 3 is close to the average. In consequence, the efficiency of this detector as well as of detector number 9 has to be lower than the average. This is a criterion not to use these detectors for calculating the final rate spectrum, as well.

In the second histogram of Figure 3.4 the comparison of detector number 5 to the average is presented. Compared to detector number 3, the two spectra are very close to each other in the whole energy range ($60 \text{ keV} < E < 350 \text{ keV}$). Only in the region between $120 \text{ keV} < E < 140 \text{ keV}$ there are small deviations from the average. Additionally this detector has a slightly higher rate than the average on the shoulder. Therefore it is concluded that this detector behaves like a normal detector.

The image of detector number 15 has a much higher rate in the low energy region than the average spectrum, and even at the end of the so called “dip region” the rate is significantly higher than the average rate. Only at the “shoulder” region the rates are nearly similar. The reason for this characteristic shape could be a hint for an abnormal high non-rejected background based on electronic disturbances with the behavior of an exponential decrease. This explains the very big difference in the low energy region and the decreasing difference in the “dip region”, as well as the equality at the “shoulder”. Despite further investigations it is not possible to clearly figure out the reason for this behavior. Detector number 16 shows a very similar form with an even higher difference at the beginning of the spectrum. According to this, these two detectors were also treated as not-normal ones, and therefore not used for the final spectrum.

In comparison to the image of detector number 3, detector number 30 shows a similar behavior and is treated as an abnormal detector for the same reasons.

3.5 Rate versus run period

In this section the rates of every run period for every single detector will be compared to each other. Therefore an energy cut with the following feature is set: every threshold energy over all run periods of one individual detector is smaller than this energy cut. Therefore the rates for different detectors vary, but for the same detector they are comparable. The rate in Figure 3.5 shows the total number of events during the run period divided by the live time for this run period. If one detector does not run, the entry for this run period is empty in the images of Figure 3.5. It is important to highlight the trend of these rates in the following Figure 3.5. In Figure 3.5 an arbitrary detector selection of detectors 4, 11, 25 and 32 is shown. The lines represent a linear fit for the slope. Thus the comparison of the detectors to each other is possible.

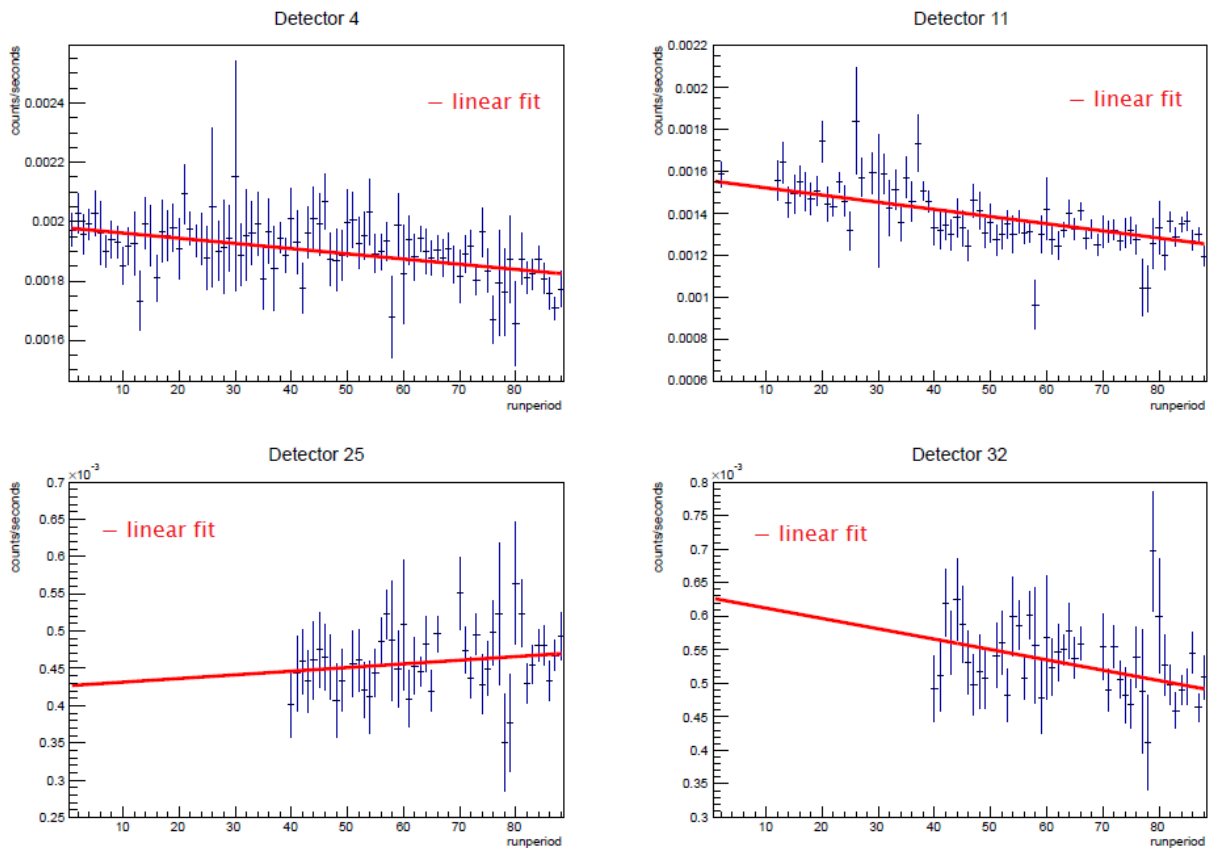


Figure 3.5: Rate versus run period for detectors 4, 11, 25 and 32

In the image for detector number 4 a regular slope is visible. This slope is a sign of a slightly decreasing rate during the whole time of about 8%, whereas the slope for detector 11 shows a much stronger decrease of about 19% during the whole 88 run periods. On the other hand there are also some detectors, especially in layer 2, where the slope shows an increase of the rate. Detector number 25 has the highest increase for all detectors over the run periods. The gain of the rate is higher than 5%. This corresponding histogram is presented in Figure 3.5.

The fourth histogram from detector number 32 again indicates a strong decrease of about 12%. For most of the detectors there seems to be a significant variation with time in the rate. The trends with their uncertainties of all detectors from layer 1 and 2 are shown in Figure 3.6. In these images the ratios of the rates between the start point and the end point of the run time of the individual detectors, based on the linear fits, are plotted¹.

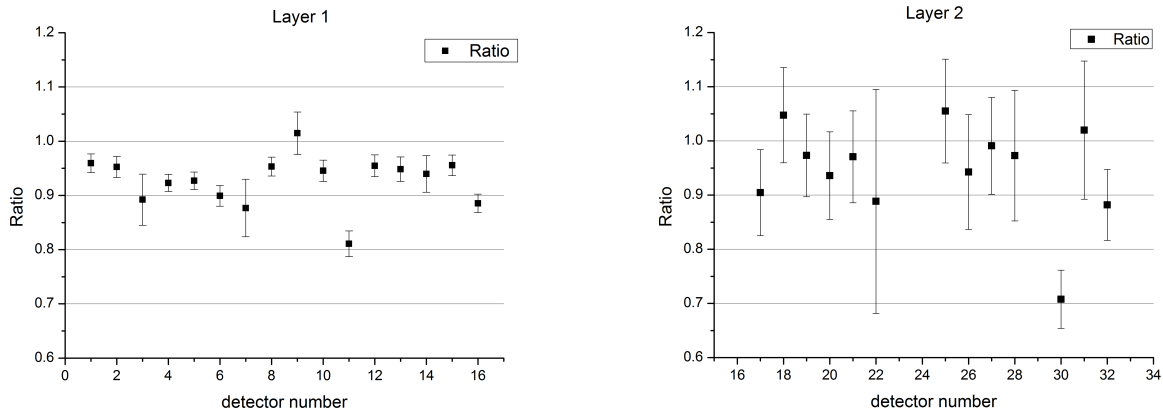


Figure 3.6: Ratio for layer 1 and layer 2

It can be seen that on average the layer 1 detectors show a bigger decrease than the detectors in layer 2 do. Only detector number 9 shows an increase of the rate, but this can also be caused by the shorter running time of this detector (this suggests to treat it as a layer 2 detector). The detector with the most significant decrease in layer 1 is number 11, which has already been described above. It is also visible that three of the layer 2 detectors show an increasing rate over time. The average² of the rate of all detectors belonging to layer 1 decrease about 7.3% and the rate for the ones belonging to layer 2 decrease about 5.5%. The reason for this behavior has not been determined so far and needs further investigations.

3.6 Final spectrum and conclusion

After all investigations under different comparison criteria, the following detector numbers are not used for creating the average spectrum: 3, 9, 13, 15, 16, 17, 20, 23 and 30. Therefore around 35 kg · days of data are included in the final spectrum. The preliminary rate spectrum is plotted red and the final rate spectrum (including only the “selected” detectors) is plotted blue in both images of Figure 3.7. In the left image all detectors are treated as one big

¹ The uncertainties were calculated based on the Gaussian propagation of uncertainty described in the appendix Equation (7.2). The respectively used uncertainties are the ones given from fitting the straight line into the rate spectra by *ROOT*.

² The decrease for the rate of the detectors is described in appendix, Table 7.3.

detector and so the error bars are very small. The same two spectra are shown in the right image of Figure 3.7. The difference is that this time the error bars indicate the variance among the individual rates of the detectors, calculated based on Equation (7.1). This highlights the reduced variation in the behavior of the selected detectors compared to the full set of detectors.

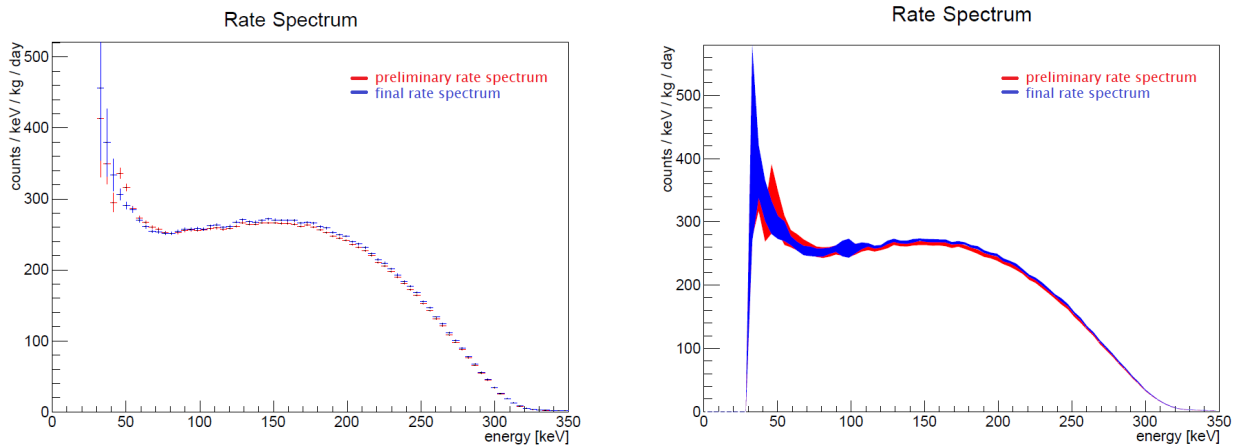


Figure 3.7: Rate Spectrum for the detectors treated as a one big detector (left) and mean spectrum (right)

In conclusion there are only small differences between the two rate spectra in the left image of Figure 3.7. The reason for this behavior is that the differences of the not included detectors compensate each other. It needs to be highlighted that the rate of the final spectrum in the “dip region” and in the “shoulder” region is slightly higher than the rate of the preliminary spectrum. Additionally the maximum at $E \approx 150$ keV for the rate of the “selected” detectors is higher than the rate of all detectors.

Furthermore for the right image of Figure 3.7 it can be noted that in the energy region from $E \approx 40$ keV to $E = 350$ keV the rate spectrum for the “selected” detectors has a smaller variance for the mean values, which was expected. It is worth mentioning that from $E \approx 120$ keV until the end of the histogram the variance for both spectra is small and decreases for higher E . The reasons for the increase of the variance in the region of $90 \text{ keV} < E < 105 \text{ keV}$ are the higher energy thresholds for layer 2 (they are in this region), and so the increase of the used data tends to increase the variance. On the whole it is visible that the shape of the spectrum for the selected detectors is more profiled. That means that the rate of the local minimum around $E = 90$ keV is smaller than on the red histogram, and the rate of the local maximum around $E = 150$ keV is higher than that for the red histogram. This indicates that the blue spectrum is in better agreement with the predicted spectrum by the theory, referring to Figure 2.3. The rate spectrum for the “selected” detectors is used for further investigations, especially for the fit to the shape predicted by the theory.

4 Results

In this chapter the results of the investigations for the data are presented. Additionally they are compared to former experimental results and the theory.

4.1 Resolution of the detectors

Based on the calibration measurements for the “selected” detectors described in Table 7.6, the following energy resolution function¹ is found²:

$$\sigma(E) = \sqrt{c + aE} = \sqrt{16.2066 + 0.117802E} \quad \text{for } E > 0 \text{ keV} \quad (4.1)$$

In this equation E and σ are in units of keV.

4.2 Shape fit

For the fit of the theoretical shape, the Equations (2.1) and (2.2) of chapter 2 section 2.1.2 “Predicted spectrum for the beta decay” are used. Additionally this shape is convoluted with a Gaussian, whose sigma represents the energy resolution of the detectors as described in

¹ The assumption for the relation of $\sigma(E) = \sqrt{c + aE}$ is based on the one hand on the intrinsic statistical detector resolution $\sigma_D(E) = \sqrt{E}$ and on the other hand of a noise contribution $\sigma_C = C$. Thus the result is $\sigma(E) = \sigma_{total}(E) = \sqrt{\sigma_D^2 + \sigma_C^2} = \sqrt{c + aE}$.

² For this calculation only the values of the “selected” detectors are included.

Equation (4.1). Additionally a constant parameter for the background is included in the fit³.

$$s(p_e) = \text{const} \cdot p_e^2 \cdot F(Z, W_e) \cdot p_\nu^2 \cdot C(p_e) + a5 \quad (4.2)$$

$$C(p_e) = p_e^6 + 7a_1 \cdot p_e^4 \cdot p_\nu^2 + 7a_2 \cdot p_e^2 \cdot p_\nu^4 + a_3 \cdot p_\nu^6 \quad (4.3)$$

$$f(E) = \int_0^{Q_\beta} s(E') \cdot R(E, E') dE' \quad (4.4)$$

$$R(E, E') = \frac{1}{\sqrt{2\pi} \cdot \sigma(E)} \exp\left(-\frac{(E - E')^2}{2\sigma^2(E)}\right) \quad (4.5)$$

where E is the kinetic energy of the electron, $p_e = \sqrt{(E + m_e)^2 - m_e^2}$, $p_\nu = Q_\beta - E$, and $W_e = \sqrt{p_e^2 + m_e^2}$. Hence, Q_β is also one of our fitting parameters. According to these four equations, the six fit parameters are: $Q_\beta = p0$, $a1 = p1$, $a2 = p2$, $a3 = p3$, $\text{const} = p4$ and $a5 = p5$.

4.3 Fit results

The fit for the energy region $50 \text{ keV} < E < 350 \text{ keV}$, based on the Equations (4.2), (4.4) and (4.5), is shown in Figure 4.1.

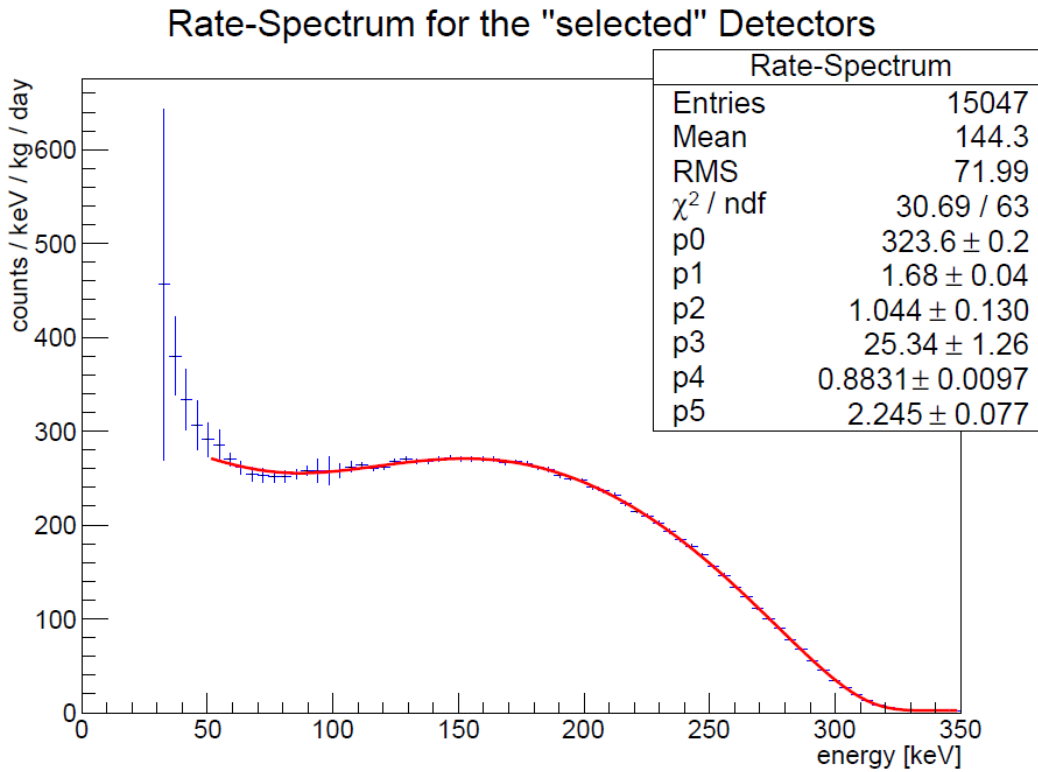


Figure 4.1: Rate spectra and fit for the beta decay of ^{113}Cd

³ In these equations $c = 1$.

The results of the fit are: $Q_\beta = (323.6 \pm 0.2(\text{stat}))$ keV, $a1 = 1.68 \pm 0.04$, $a2 = 1.04 \pm 0.13$ and $a3 = 25.13 \pm 1.26$. The fit result for the normalization factor⁴ is $const = (3.565 \pm 0.039) \cdot 10^{-25}$. The constant background is $a5 = 2.245 \pm 0.077$. Using the chi-squared distribution as a measure for the goodness of the fit ($\chi^2/\text{ndf} = 30.69/63$), it indicates that the theoretical model describes the data very well but shows a tendency of over fitting ($\chi^2/\text{ndf} < 1$). However the difference of the measured χ^2 from its expectation value is still in the 3σ range, referring to Equation (7.3) and (7.4).

In the ‘‘shoulder’’ region ($150\text{keV} < E < 350$ keV) the fit is in good accordance to the spectrum. The differences between the fit and the data are also quite small in the ‘‘dip region’’. Only at the beginning at the low energy region ($50\text{keV} < E < 80$ keV) there is a small divergence between the rate spectrum and the fit. In general the fit is in very good accordance to the data in the region for $50\text{keV} < E < 350$ keV and the $Q_\beta = (323.6 \pm 0.2(\text{stat}) \pm 1.2(\text{sys}))$ keV. The last uncertainty is the systematic one, which is caused by the energy calibration, referring to Table 7.7. In conclusion this result is in good accordance to $Q_{\beta_{\text{theory}}} = (322.6 \pm 0.8)$ keV and overlaps with the theoretical value, referring to chapter 2 section 2.2.1 ‘‘Experimental results’’.

4.4 Half-life

The decay constant λ and $T_{\frac{1}{2}}$ for the beta decay is calculated by the following formulas according to [BJ69]:

$$\begin{aligned}\lambda &= \frac{g^2}{2\pi} \int_0^{p_0} p_e^2 \cdot (W_0 - W_e)^2 \cdot F(Z, W_e) \cdot C(W_e) dp_e \\ \lambda &= const \cdot \int_0^{p_0} p_e^2 \cdot F(Z, E) \cdot p_\nu^2 \cdot C(p_e) dp_e \\ T_{\frac{1}{2}} &= \frac{\ln(2)}{\lambda}\end{aligned}\tag{4.6}$$

where $p_0 = \sqrt{W_0^2 - m_e^2}$ and $const$ is a normalization factor and $p_e^2 \cdot F(Z, E) \cdot p_\nu^2 \cdot C(p_e)$ is the theoretical shape function. According to the fit results, the integral has the following form:

$$\lambda_{\text{fit}} = (66.832 \pm 0.734) \frac{1}{\text{g} \cdot \text{day}}$$

The uncertainty for λ_{fit} is based on the uncertainty of the $const$ given by the fit. All uncertainties are calculated based on Gaussian propagation of uncertainties, referring to Equation (7.2).

For creating the rate spectra, the total mass of a single detector is used. Hence it is important

⁴ The factor of $4.037 \cdot 10^{-25}$ has already been pre-implemented in the program for the fit. Therefore the result is $const = 0.8831 \cdot 4.037 \cdot 10^{-25}$.

to know the absolute mass of ^{113}Cd for the detectors. For every detector's unit the number content is $\text{Cd}_{91}\text{Zn}_9\text{Te}_{100}$ with $M_{\text{Det}} = 23578.1 \frac{\text{g}}{\text{mol}}$, referring to Table 7.1. Additionally in natural cadmium the number of the isotope ^{113}Cd is $(12.22 \pm 0.12)\%$, referring to Table 7.1. Thus the ratio of the number of ^{113}Cd atoms to the total number of atoms in 1 g of the detector is:

$$r = \frac{0.1222 \cdot 91 \cdot N_{\text{A}}}{M_{\text{Det}}} = (2.840 \pm 0.068) \cdot 10^{20}$$

where $N_{\text{A}} = 6.02214129 \cdot 10^{23} \frac{1}{\text{mol}}$ is the Avogadro constant. The uncertainty for r comes from the uncertainty of the number of cadmium in one unit, which is ± 2 , referring to [BDSKZ]. The λ_{fit} has to be divided by the factor r to get the counts which accord to the mass of 1 g. Furthermore the unit of the y-axis is counts per day per kg, the half-life is in years, so the factor $t = 365.25$ is included, too. Another factor is the so called efficiency factor $e = 0.98 \pm 0.01$. This is important since through the “z-cut” the events under a lower limit of the z-distribution were not included for further calculations according to chapter 3 section 3.2.1 “Z-distribution”. On the whole λ is calculated by the following formula:

$$\lambda = \lambda_{\text{fit}} \cdot \frac{1}{e \cdot r} \cdot t = (8.764 \pm 0.096(\text{stat}) \pm 0.228(\text{sys})) \cdot 10^{-17} \frac{1}{\text{year}}$$

In this calculation the uncertainties of r as well as e are used for the systematic uncertainty. The uncertainty of the fit represents the statistic uncertainty for $T_{\frac{1}{2}}$. Hence $T_{\frac{1}{2}}$ is given by $T_{\frac{1}{2}}(^{113}\text{Cd}) = (7.909 \pm 0.087(\text{stat}) \pm 0.205(\text{sys})) \cdot 10^{15}$ years, according to Equation (4.6). On the whole the fit spectrum has the following shape (Figure 4.2):

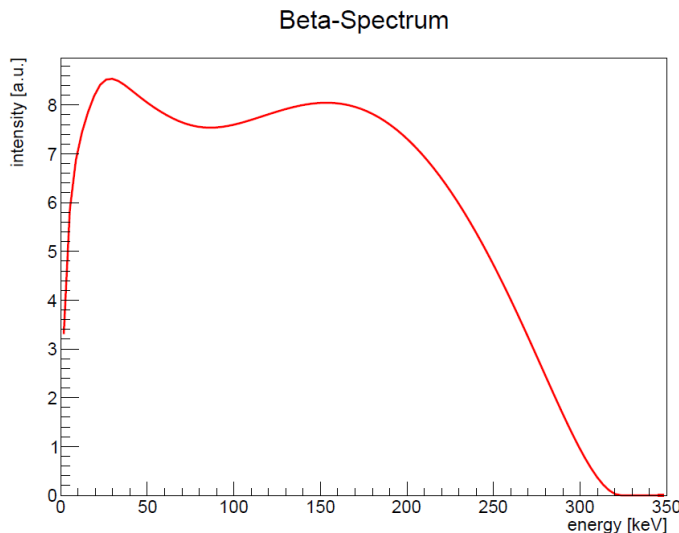


Figure 4.2: Spectrum based on the fit

This shape shows significant differences in comparison to other experimental results, referring to the right image of Figure 4.3. The biggest variances are in the so called low energy region ($0 \text{ keV} < E < 80 \text{ keV}$). In all other experimental results the rate increases strictly monoton-

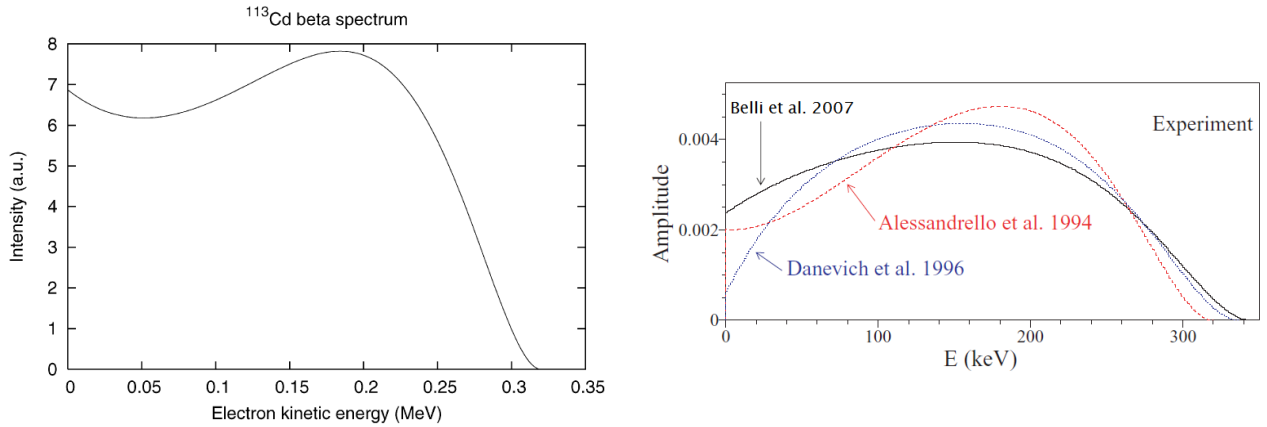


Figure 4.3: Shape predicted by the theory [MS07] (left) and experimental results [PB07] (right)

ically from $E = 0$ keV to the maximum at around $E \approx 150$ keV, referring to the right image of Figure 4.3. The rate in Figure 4.2 has a strong increase from $0 \text{ keV} < E < 30$ keV. There is a global maximum at $E = 30$ keV. After the maximum the rate decreases to $E \approx 70$ keV for a local minimum. For $70 \text{ keV} < E < 160$ keV the rate increases again to a local maximum and after this the rate decreases to zero until $E = Q_\beta$. In conclusion the difference between the rate of Figure 4.2 and the rate in the right image of Figure 4.3 is that the first rate has a local minimum with two local maxima. Additionally the rate decreases to zero for $E = 0$ keV in Figure 4.1, whereas the rate in the right image of Figure 4.3 already has a high rate for $E = 0$ keV. In comparison to the other experimental results for the shape, this shape agrees most to the shape predicted by the theory, referring to the left image of Figure 4.3. There are still some differences, but both profiles have similarities. Therefore the spectrum of the selected detectors is close to the theoretical one, excluding the low energy region $0 \text{ keV} < E < 30$ keV. However, in general the fitted spectrum is in good accordance with the theoretical one.

4.5 Conclusion

The results of the fit are very satisfying. The Q_β -value is in nearly perfect agreement to the theoretical value. Additionally the half-life shows a very good accordance to other experiments for ^{113}Cd , referring to chapter 2 section 2.2.1 “Experimental results”. The shape of this beta decay spectrum is quite different in the low energy region in comparison to the other experimental result, but it is comparable to the theory, according to the left image of Figure 4.3. Overall, the data from the selected detectors represent the theoretical estimation very well, and reproduce former experimental results, too.

5 Summary and outlook

In this thesis the experimental results for the fourfold forbidden, non-unique beta decay of ^{113}Cd have been studied. All 32 detectors of the COBRA experiment have been investigated for different comparison criteria. In this thesis around 50 kg·days of data have been analyzed. The results which are produced are quite promising. For the endpoint of the spectrum it is found that $Q_\beta = (323.6 \pm 1.2)$ keV and the half-life is $T_{\frac{1}{2}}(^{113}\text{Cd}) = (7.909 \pm 0.223) \cdot 10^{15}$ years. Both characteristic values are in a nearly perfect agreement to the ones measured by other experiments. Moreover the shape of this beta spectrum fits well to the latest theory.

Nevertheless there are several points for further investigations. In this thesis the fit for the rate spectrum has been only done down to an energy of $E = 50$ keV. The more interesting region is the region between $0 \text{ keV} < E < 50 \text{ keV}$. The rate, and therefore also the spectrum, is more significant for verifying the theory. However it is a great challenge to measure the spectrum in this low energy region very precisely, because there is normally a very high background caused by electronic disturbances. This can also have a great impact on the calculation of the half-life.

Another point for further investigations is the high systematic uncertainty of the result in comparison to the statistical one. Hence the investigation of systematic uncertainties could have a higher priority in the future. One of the biggest uncertainties is caused by the not precisely enough defined content of cadmium in the detectors. Therefore the next step could be to find a method for a more precise measurement of the content for cadmium.

On the whole the COBRA experiment is appropriate for beta decay spectrum studies of ^{113}Cd because the results are very exact within small uncertainties in the region above $E = 50$ keV. Hence the current setup of the experiment is a very good base for further investigations in this research field.

6 References

6.1 Books and papers

- [AMDFZ] M Fritts, J Durst, T Göpfert, T Wester, K Zuber, Analytical model for event reconstruction in coplanar grid CdZnTe detectors. Nucl. Instrum. and Methods in Physics Research Section A 708 (2013), pp. 1-6
- [AME03] G. Audi, A. H. Wapstra and C. Thibault, Nucl. Phys. A 729, 337 (2003)
- [BD94A] A. Alessandrello et al., Nucl. Phys. B, Proc. Suppl. 35, 394 (1994)
A. Alessandrello et al., Nucl. Instrum. Methods A 344, 243 (1994)
- [BDSKZ] An Investigation into the ^{113}Cd Beta Decay Spectrum using a CdZnTe Array, J. V. Dawson, Zuber, 2009
- [BJ69] H. Behrens and J. Janecke, Numerical Tables for Beta-Decay and Electron Capture (Springer-Verlag, Berlin, 1969)
- [CPG95] P. Luke, IEEE Trans. Nucl. Sci. 42, 4 (1995)
- [FAD96] F. A. Danevich et al., Phys. At. Nucl. 59, 1 (1996)
- [MS07] M. T. Mustonen, M. Aunola, and J. Suhonen, Phys. Rev. C 73, 054301 (2006); 76, 019901(E) (2007)
and M. T. Mustonen and J. Suhonen, Phys. Lett. B657, 38 (2007)
- [PB07] Belli et al, Phys. Rev. C 76, 064603 (2007)

- [RCOB09] C. J. Reeve. Data Analysis and Background Studies for the COBRA Neutrinoless Double-Beta Decay Experiment. PhD thesis, University of Dortmund, 2009
- [SH66] H. Schopper, Weak interactions and nuclear beta decay (North Holland Publishing Co, Amsterdam, 1966)

6.2 World Wide Web

The last call of all websites was 6:20 pm on June, 7th.

- [AME12] <http://amdc.impcas.ac.cn/evaluation/data2012/data/mass.mas12>
- [CaIic] <http://www.internetchemie.info/chemiewiki/index.php?title=Cadmium-Isotope>
- [CEORG] <http://www.cobra-experiment.org/>
- [evDet] eV-PRODUCTS, <http://www.evproducts.com>
- [Fgobd] <http://lightestisotope.files.wordpress.com/2009/10/betadecay.png%3Fw%3D450>
- [LCoNCd] <http://www-nds.iaea.org/relnsd/vcharthtml/VChartHTML.html>
- [ToICd] <http://ie.lbl.gov/toi/nuclide.asp?iZA=480113>
- [ToIalb] <http://ie.lbl.gov/decay/betas/BM480113.htm>
- [wbeta] <http://en.wikipedia.org/wiki/Beta-particle>
- [wcadm] <http://de.wikipedia.org/wiki/Cadmium>
- [wneum] <http://en.wikipedia.org/wiki/Neutrino>
- [wtell] <http://de.wikipedia.org/wiki/Tellur>
- [wzink] <http://de.wikipedia.org/wiki/Zink>

7 Appendix

In this chapter formulas for statistics, the formula for uncertainties, tabulated values for the Fermi function and some tables for describing the properties of the detectors are presented.

7.1 Formulas for statistics

For N measurements of quality x there is:

$$\begin{aligned}\bar{x} &= \frac{1}{N} \sum_{i=1}^N x_i && \text{the mean value} \\ V(x) = \sigma(x)^2 &= \frac{1}{N-1} \sum_{i=1}^N (x_i - \bar{x})^2 && \text{the variance of } x \\ V(\bar{x}) = \sigma(\bar{x})^2 &= \frac{(\sigma(x))^2}{N} && \text{the variance of } \bar{x}\end{aligned}\tag{7.1}$$

In this equation $V(x)$ is the variance for the quality x and $\sigma(x)$ is the standard deviation for the quality.

7.2 Formula for Gaussian propagation of uncertainties

For a function $f(x) = f(x_1, x_2, \dots, x_N)$ with the single uncertainties Δx_i the complete uncertainty of $f(x)$ is defined as the following equation (under the disregard of correlations):

$$\Delta f(x) = \sqrt{\sum_{i=1}^N \left(\frac{\partial f(x)}{\partial x_i} \right)^2 (\Delta x_i)^2}\tag{7.2}$$

7.3 Fit parameters

The following two equations describe the connection between the two important fit parameters χ^2 and ndf (number of degrees of freedom):

$$\langle \chi^2 \rangle = \text{ndf} \quad (7.3)$$

$$V(\chi^2) = 2 \cdot \text{ndf} \quad (7.4)$$

where $\langle \chi^2 \rangle$ is the expectation value of χ^2 and $V(\chi^2)$ is the variance of χ^2 .

7.4 Table 7.1 – Masses for the natural elements of the detectors

In Table 7.1 the masses of natural elements, which the detectors include, are listed; additionally the natural abundance of ^{113}Cd in natural Cd is listed:

Element	mass [$\frac{\text{g}}{\text{mol}}$]	Source
Cd	112.411	[wcadm]
Zn	65.409	[wzink]
Te	127.60	[wtell]
Isotope	abundance in natural element Cd [%]	Source
^{113}Cd	12.22 ± 0.12	[Calic]

Table 7.1: Masses of natural elements

7.5 Table 7.2 – Masses of the detectors

In Table 7.2 the masses of the individual detectors are shown¹.

Detector number	mass [g]	Detector number	mass [g]
1	5.9002	17	5.8690
2	5.8887	18	5.8738
3	5.8509	19	5.8776 *
4	5.9063	20	5.8771
5	5.8578	21	5.8664
6	5.8776 *	22	5.8536
7	5.8330	23	5.9046
8	5.8524	24	6.4590
9	5.8930	25	5.8776 *
10	5.9046	26	5.8776 *
11	5.8776 *	27	5.8776 *
12	5.9029	28	6.5290
13	5.8607	29	5.8776 *
14	5.9064	30	5.8597
15	5.8667 *	31	5.8853
16	5.9053	32	5.8669
Average		5.9161 g	
Variance		0.0234 g	

Table 7.2: Masses of the detectors

¹ The masses with the asterisk * are unknown and were calculated by the mean value of the known light detectors (all with a mass smaller than 6 g), because it is known that these belong to them.

7.6 Table 7.3 – Rate trends of the detectors

Table 7.3 shows the change of the rate for every single detector. In the table the ratio of the end rate divided by the beginning rate and the uncertainty is given².

Detector number	ratio	uncertainty	Detector number	ratio	uncertainty
1	0.959	0.017	17	0.905	0.079
2	0.952	0.019	18	1.047	0.088
3	0.892	0.047	19	0.973	0.076
4	0.923	0.016	20	0.936	0.081
5	0.927	0.016	21	0.971	0.085
6	0.899	0.019	22	0.888	0.207
7	0.877	0.053	23	*	
8	0.953	0.017	24	*	
9	1.015	0.039	25	1.055	0.096
10	0.945	0.020	26	0.943	0.106
11	0.811	0.024	27	0.991	0.089
12	0.955	0.020	28	0.973	0.121
13	0.948	0.023	29	*	
14	0.940	0.034	30	0.708	0.054
15	0.956	0.019	31	1.020	0.128
16	0.885	0.017	32	0.882	0.065
Average layer 1			0.9274		
Average layer 2			0.9455		

Table 7.3: Rate trends of the individual detectors

² The detectors with the asterisk * have at least one run period with an energy threshold higher than $E = 350$ keV. For this reason they are not included.

7.7 Table 7.4 – Tabulated values of the Fermi function

In Table 7.4 the values for the Fermi function based on the screened β -decay Coulomb function for certain energies E are listed, according to [BJ69]. The values for the screened Coulomb function is used, because for ^{113}Cd the screening of the electrons becomes more and more important. In Figure 7.1 the spline of these values is shown.

E [keV]	W [$m_e c^2$]	p [$m_e c$]	$F(49, W)$
2.55	1.005	0.1	51.5392308
10.12	1.020	0.2	26.0535418
22.50	1.044	0.3	17.6699108
39.36	1.077	0.4	13.5723735
60.32	1.118	0.5	11.1978655
84.92	1.166	0.6	9.6814698
112.76	1.221	0.7	8.6581507
143.40	1.281	0.8	7.9177285
176.48	1.345	0.9	7.3736760
211.67	1.414	1.0	6.9573339
287.21	1.562	1.2	6.3662275
368.16	1.720	1.4	5.9715843
453.16	1.887	1.6	5.6828692
541.22	2.059	1.8	5.4773072

Table 7.4: Tabulated values for the Fermi function

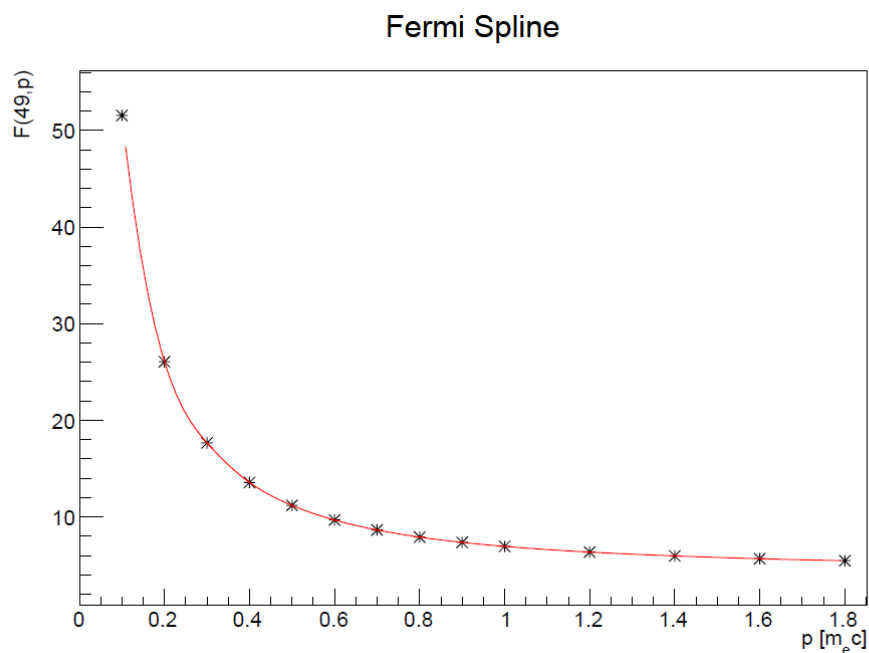


Figure 7.1: Spline of the Fermi function

7.8 Table 7.5 and 7.6 – Resolution of the detectors

In Table 7.5 and 7.6 the resolution of the detectors are shown. In the tables the average of twelve (layer 1) and five (layer 2) measurements for each detector³ for $E = 239$ keV and $E = 511$ keV and the average of them⁴ are listed.

$E = 239$ keV			
Detector number	σ [keV]	Detector number	σ [keV]
1	7.9852	17	8.5103
2	6.6976	18	6.2349
3	9.0586	19	5.9551
4	8.2811	20	9.1860
5	5.9085	21	6.2308
6	7.0327	22	6.6589
7	5.8822	23	6.0722
8	5.6233	24	8.6471
9	6.6888	25	6.9231
10	4.5622	26	5.7640
11	5.8901	27	6.0645
12	5.7225	28	8.1648
13	7.7903	29	7.9509
14	7.2092	30	7.8881
15	6.2024	31	6.4680
16	8.9288	32	6.2349
Average		8.7409	

Table 7.5: Resolution of the detectors for $E = 239$ keV

³ In the following dates the calibration was done for layer 1: 2011-09-29, 2011-11-07, 2011-11-11, 2011-12-06, 2012-02-09, 2012-03-23, 2012-07-23; for both layer 1 and 2: 2012-04-04, 2012-07-19, 2012-08-14, 2012-09-11, 2012-12-02.

⁴ The average does not include the detectors with some kind of electronic disturbances. For further information see chapter 4.

$E = 511$ keV			
Detector number	σ [keV]	Detector number	σ [keV]
1	10.5155	17	11.1546
2	8.7119	18	7.8071
3	11.0695	19	7.4188
4	10.3920	20	11.4400
5	7.3323	21	7.7239
6	8.9673	22	8.1365
7	8.0221	23	8.0397
8	7.1709	24	14.5056
9	11.7757	25	8.8598
10	5.9283	26	6.9729
11	8.6535	27	7.5327
12	7.3406	28	12.9641
13	9.7326	29	10.1784
14	8.6874	30	10.3553
15	7.5513	31	7.6705
16	10.6607	32	9.5486
Average		8.7409	

Table 7.6: Resolution of the detectors for $E = 511$ keV

7.9 Table 7.7 – Energy calibration uncertainties of the detectors

In Table 7.7 the uncertainties for the energy calibrations of the detectors are listed. In the table the average of twelve (layer 1) and five (layer 2) measurements for each detector⁵ for $E = 323.6$ keV (this is the Q_{β} -value accord to chapter 4) and the average of them⁶ are listed.

$E = 323.6$ keV			
Detector number	Calibration- uncertainty [keV]	Detector number	Calibration- uncertainty [keV]
1	1.02	17	1.21
2	1.48	18	1.27
3	1.92	19	1.03
4	1.70	20	2.13
5	0.74	21	0.75
6	0.97	22	1.12
7	0.69	23	1.00
8	0.80	24	3.87
9	1.84	25	0.86
10	0.70	26	0.74
11	1.62	27	1.17
12	0.97	28	1.58
13	1.30	29	1.07
14	0.93	30	1.52
15	0.86	31	1.10
16	1.38	32	0.58
Average		1.16	

Table 7.7: Energy calibration uncertainties of the detectors

⁵ On the following dates the calibration was done for layer 1: 2011-09-29, 2011-11-07, 2011-11-11, 2011-12-06, 2012-02-09, 2012-03-23, 2012-07-23; for both layer 1 and 2: 2012-04-04, 2012-07-19, 2012-08-14, 2012-09-11, 2012-12-02.

⁶ The average does not include the detectors with some kind of electronic disturbances. For further information see chapter 4.

Erklärung

Hiermit erkläre ich, dass ich diese Arbeit im Rahmen der Betreuung am Institut für Kern- und Teilchenphysik ohne unzulässige Hilfe Dritter verfasst und alle Quellen als solche gekennzeichnet habe.

Fabian Heiße

Dresden, Juni 2013